

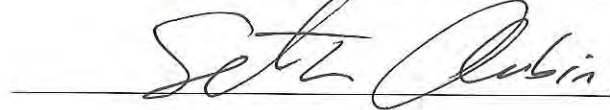
# Fluid Dynamics Measurements for Blade Designs

A thesis submitted in partial fulfillment of the requirement for the degree of Bachelor of Science in Physics  
from The College of William and Mary

Jack Jackson

A blue ink signature, likely of Prof. Bill Cooke, written over a horizontal line.

Advisor: Prof. Bill Cooke

A black ink signature, likely of Seth Aubin, written over a horizontal line.

Senior Research Coordinator: Seth Aubin

Department of Physics  
College of William and Mary  
Williamsburg, Virginia  
May 3, 2019

## **Acknowledgements**

I would like to thank Professor Cooke for helping to keep me focussed on the process of the experiment whenever I was looking too far in the future. Also, for demonstrating the importance of the “quick and dirty” experiment to get a better grasp of the validity of our goals. I should also thank Professor Saskia Mordjick for working with me in my understanding of the fluid dynamical processes possible with the experiment. Her guidance and knowledge was invaluable to my understanding of the project. Finally, I would like to thank Vincent Cordrey for his help with coding and algorithm writing. The encouragement and teaching he provided allowed for significant progress in my ability to analyze data more efficiently.

## Abstract

Aqua farmable algae offers environmental benefits to the local waterways. In order to more effectively harvest algae from a substrate with minimal disturbance to growth rate, it is important to somehow trim the algae without removing it from the water. The problem then becomes one of fluid dynamics and the laminar flow associated with the algae. Research must be done to find the blade design that possesses the correct hydrodynamic properties in order to effectively cut the algae. In order to make the necessary measurements, it is important to be able to make accurate measurements with the given equipment. Our equipment included a GoPro Hero 3+ Black Edition with a fish-eye lens. Fish-eye lenses distort true distances of an image in order to incorporate a wider field of view. We found a master equation for how distances within an image of zero degree tilt can be accurately measured in air. Moving the camera into the water had the effect of linearizing the image. Any distance left to right in a given frame of video can be classified on the order of the reciprocal of the distance the camera lens is from the target plane. Shining a laser along the edge of the submerged oscillating blade allowed us to record video of rosin particles' motion caused by the resulting flow. The resulting velocities helped us to characterize flows in a given time period as turbulent.

## 1 Introduction

In the late 2000's to early 2010's, a project for growing algae for the purpose of a bio-fuel source was created at William and Mary. At the time gasoline cost around \$4.00 per gallon, and the members of the research team believed they could produce a viable gasoline alternative of comparable price. Since gasoline prices have dropped in the last decade, the primary motivation for the project has changed to one of ecological restoration.

Water based algae farms provide a medium in which municipalities can offset their Total Maximum Daily Load (TDML). A locality's TDML as defined by the United States Clean Water Act, identifies the maximum amount of pollutants a body of water can have and still meet standards. Algae is a viable scrubber of phosphates and nitrogen from water ways and the opportunity to farm the algae with low surface area impact allows for an economically viable way to clean the Chesapeake Bay. After the growth of the algae, an efficient harvesting method would also allow for an increased number of waterman jobs due to the roughly weekly harvest time requirements.

The research group was able to grow algae colonies on constructed barges with eight vertical screens beneath. With the help of VIMS (Virginia Institute of Marine Science), the group was able to float the barge to a location in the York River and grow algae at a highly significant rate. The issue turned from one

of growth to one of harvest. Initially, harvesting occurred by manually removing the screens from the water and scraping algae from the screens. This proved not only to be slow and labor intensive but had a serious negative affect on the regrowth rate of the algae, as the root like structure that adhered the algae to the screen was often collateral damage. This “uprooting” also allowed an increase in biofouling (the growth of non-algae).

In order to effectively harvest the algae while maximizing the growth rate, the group decided it was necessary to harvest in water without damaging the attachment of the algae to the substrate. Previous research showed the most effective method would be trimming the algae as it was submerged. The researchers tried different methods of harvesting including, water-pick, electricity, and manual blades. They found the oscillating blade to be the most effective, however the successful cut rate was very low. The fine structure of the algae caused it to be a part of the boundary layer flow of the water over the blade. Simply put, the algae slid over the blade as if it were the water. In order to successfully cut the algae in water, it is important to have the correct mix of laminar flow and turbulence. This poses a fluid dynamics problem which must be investigated.

In order to carry out these investigations, we are using the 240 frames per second (fps) video mode on a GoPro Hero 3+ Black Edition camera. The setup, shown in Figure 1, was used to image the top of an oscillating blade in water. The camera’s lens is still submerged in such a manner as to record test particle movement above an oscillating blade while simultaneously capturing images below. Using combinations of particle tracking, area, and brightness, we are able to obtain fluid dynamic measurements in two dimensions and extrapolate the information of the depth dimension. The experimental setup required precise knowledge of how the fish-eye distorts distances in air as well as in water, with the water attributes being the most critical for our experiment.

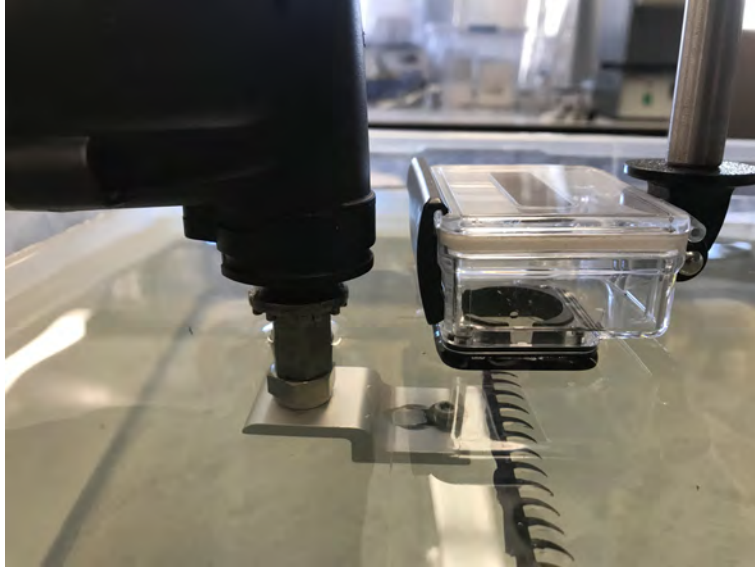


Figure 1: This is a side view of the in water experimental setup. Both the test blade and the camera lens, represented by the black band on the camera case, are submerged.

In order to use this model camera to make the measurements that we desire, we must first understand the characteristics of the curvature associated with the GoPro's fish-eye lens. The Hero 3+'s fish-eye lens is a  $f/2.8$  6-element aspherical glass lens. The  $f/2.8$  refers to the camera's  $f$ /stop number. An  $f$ /stop is simply the ratio of the focal length and the diameter of the lens. This is equivalent to a  $50\text{ mm}$  focal length lens having an aperture of  $17.86\text{ mm}$ . With an  $f$ /stop of 2.8, the Hero 3+ Black has a more limited depth of field than higher  $f$ /stop numbered cameras, thus allows for a more focused center of an image than the background.

The camera's aspherical lens has advantages and one minor disadvantage. An aspheric lens is a lens not based on spherical surfaces. The use of an aspherical lens, shown versus a spherical lens in Figure 2, has the advantage of correcting spherical aberration, the optical effect of incident light rays focusing at different points, causing blurring in an image as illustrated in figure 2.

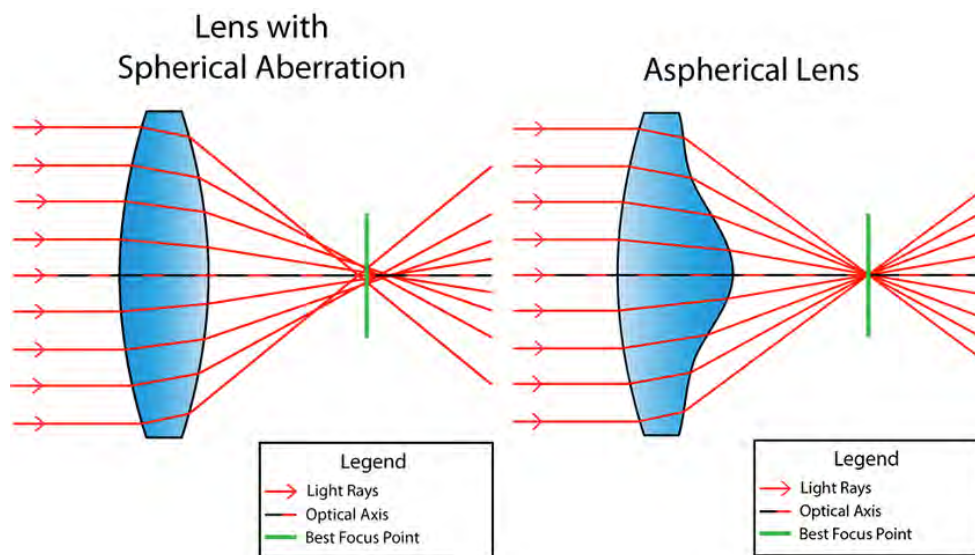


Figure 2: Spherical aberration correction of a normal lens (left) and an aspherical lens (right). Reference 1.

The aspheric lens is able to focus most of the light into a small area, thus creating a sharper image. Also, as the image spreads out from the center, the distance in the image becomes smaller, though not as quickly as a perfectly spherical lens. The disadvantage in use of these lenses is the difficult curvature involved in the lens. A spherical lens has a uniform curvature for the surface of the lens where as an aspherical lens has a more complicated surface profile. We needed to understand how the complicated shape affected distances measured across the plane of an image without necessarily needing to know the exact curvature of the lens.

Once we understood how the image distortion behaved in our experimental setup, we had to understand what fluid dynamic problems we would face. Fluid flow where the local velocity is tangent to the direction of flow is known as a streamline. When inspecting a specific “particle” of fluid in the flow, the term used is a pathline. In cases of steady flow, these two trajectories are the same. In the case where the flow pattern changes over time, the pathline will deviate from the streamline due to the time dependence of the flow. We hoped to map specific pathlines to obtain velocity measurements which we could in turn use to understand the flow patterns, laminar versus turbulent.

Laminar flow, sometimes referred to as streamline flow, occurs when a fluid flows in parallel fashion. There are neither parallel flows, nor eddies, swirls in the fluid. The flow is also described by a low Reynolds number, the ratio of inertial forces to shearing forces or viscosity. Any number below 2300 is in the strictly laminar region. One calculates a basic Reynolds number by  $Re = \frac{\rho \cdot \vec{V} \cdot L}{\mu}$  where  $\rho$  is density of the fluid,  $\vec{V}$  is the velocity vector,  $L$  is the length through which the fluid flows, and  $\mu$  is the dynamic viscosity of the fluid. In contrast, turbulent flows occur when the inertial forces dominate the viscosity of a fluid. A Reynolds number above 4000 is in the turbulent domain with a flow pattern characterized by eddies and vortices. However for total turbulence that could be described as “pure turbulence” or chaotic motion, the Reynolds number is on the order of  $10^6$ . Between 2300 – 4000 and the flow is considered transient. Any evidence of these eddies, coupled with Reynolds values and velocities would allow classification of flows near the oscillating blade.

## 2 In Air Image Procedure

Earlier research done in the summer of 2018 assumed the curvature was dependent on a cubic function. We took images and overlaid concentric circles about the perceived center on graph paper based upon an  $f(x) = A \cdot r(1 - r^2)$  function. The goal was find a general function for curvature as a function of distance with one adjustable parameter,  $A$ . We believed if we could find a relationship between the  $A$  parameters for each measured distance, we could then map these concentric circles to images from any distance, and have accurate measurements of distances in the fish-eye distorted image. The first challenge was to find the center of the image and have as close to zero tilt about the vertical axis so we could plot concentric circles representing 5mm distance in real space, as deviations from the center would result in the concentric circles not landing on major hash crossings. Figure 3 illustrates an example of nearly zero degree tilt in an image.

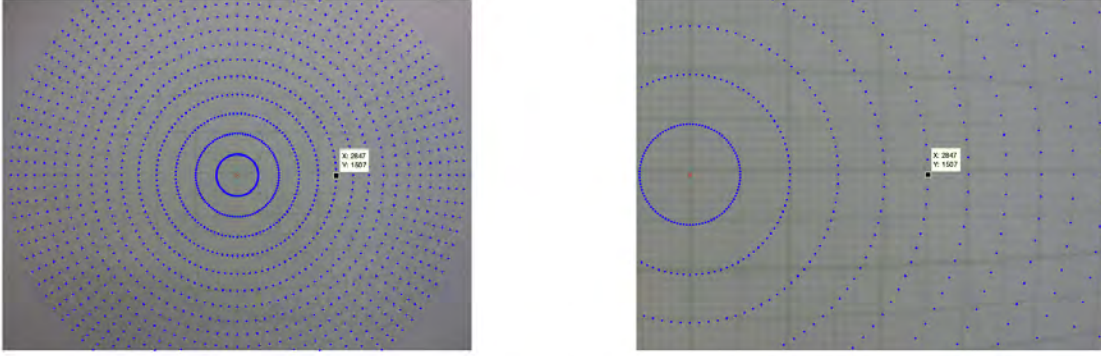


Figure 3: These are examples of an almost zero degree tilt. The images illustrate the accuracy of the rings overlaid upon the 5 *mm* lines on the graph paper. The highlighted point is the same in both images. **Left:** Full View. **Right:** Zoom-in for reference.

As seen in the preceding figure, at 37 *mm* from the target plane, for a  $0^\circ$  tilt, the concentric circles fell very closely on the 5 *mm* major lines of the graph paper, and we were able to tell quickly how much deviation occurred in an angular shift from zero, which can be seen in Figure 4, where the rings are no longer aligned with hash marks.

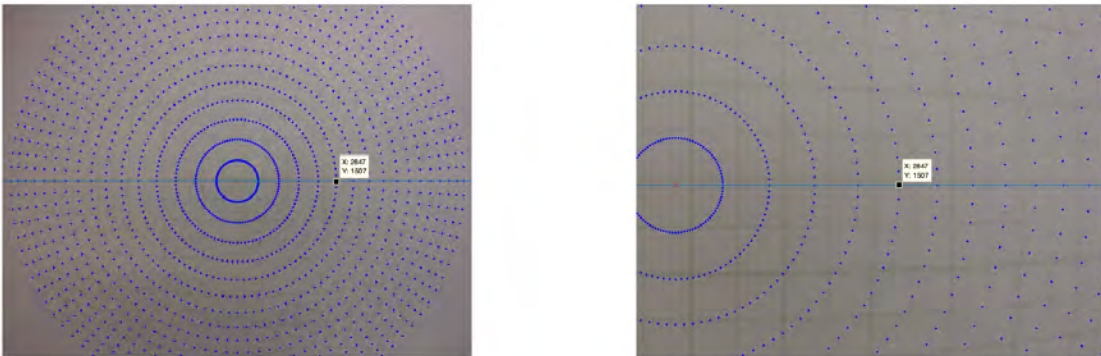


Figure 4: These are examples of a  $-1.5^\circ$  tilt from zero. The rings are no longer aligned with every major 5 *mm* line on the graph paper. The highlighted point is the same in both images. **Left:** Full View. **Right:** Zoom-in for reference.

We quickly found the  $r^3$  function to be incorrect, as distances between the outer circles shrunk too quickly. Next we tried  $f(x) = A \cdot r(1 - r)$ , which worked extremely well for close distances from the camera



to the target plane, but the accuracy would degrade in the intermediate circles as the distance increased, only to then realign with predicted values as the outer circles were plotted. In an effort to improve on the positions of the intermediate points, the fit function was expanded to  $R = Ar + Br^2 + Cr^3 + Dr^4 + Er^5$  with expected values of zero for the even coefficients. However, the plotted circles most accurately fit the vertical hashes when each coefficient had a non-zero value. Figure 5 shows the  $r^5$  fit concentric circles and how well they match the 5 *mm* major hash lines as the circles are overlaid from the center point for the closest and farthest distances measured respectively.

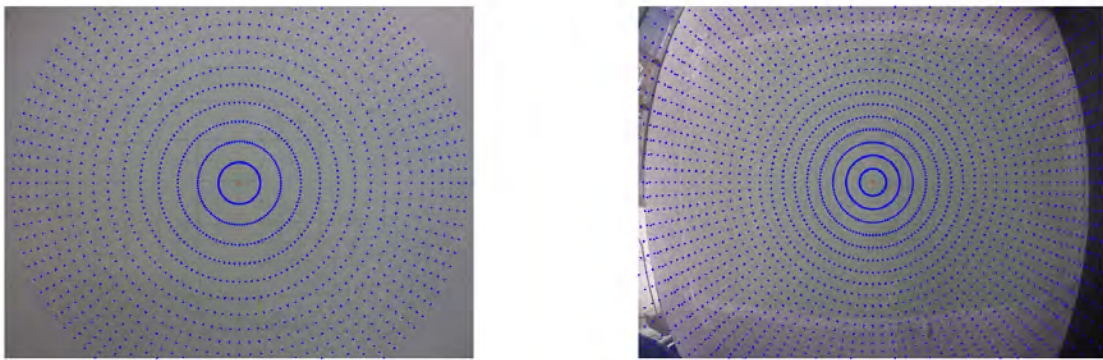


Figure 5: These are approximate zero degree tilt of the  $r^5$  function at a distance of 37 millimeters from the target (left) and 148 *mm* (right). The function was of the form  $R = Ar + Br^2 + Cr^3 + Dr^4 + Er^5$ . Each circle is plotted to have a radius 5 *mm* greater than the one preceding.

Finally, we changed the procedure to finding pixel values for 5 *mm* increments along the horizontal axis located along the center of the image and plotted their positions. This was a faster way to find the characteristics of lens, since we did not have to immediately take into account any tilt. A visual estimate of zero degrees was sufficient, without having to plot any circles and guess what type of function would overlay the circles properly. We could simply examine the raw data.

Each data point represented a 5mm distance in real space, making it easy to calculate distances and pixels per 5 *mm*. We now had a conversion between pixels and distance that we could interchange to better understand the curvature of the fish-eye image.

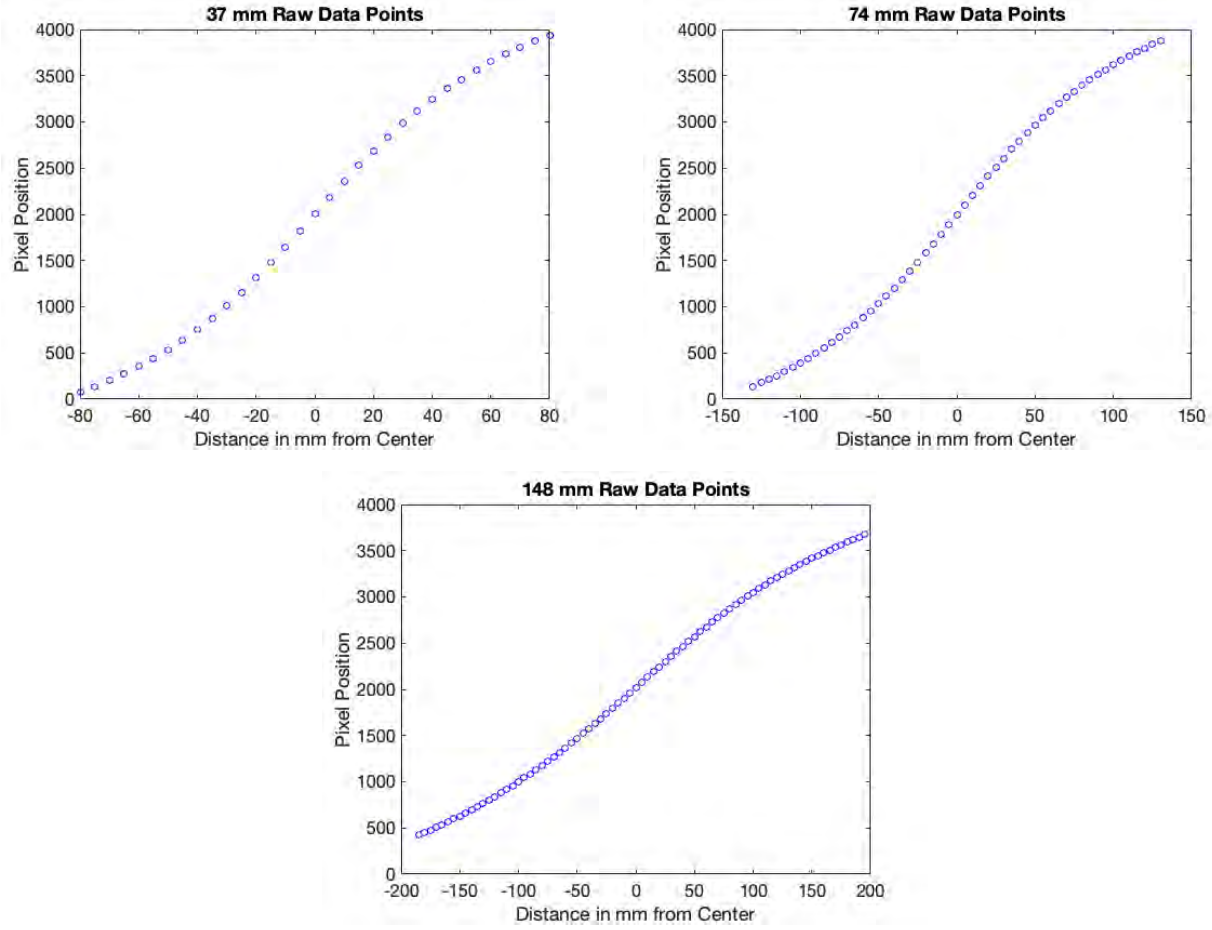


Figure 6: The raw data from each of the measured distances show an  $r^5$  dependence which could possibly be estimated by a function with less adjustable parameters.

The plots in Figure 6 confirmed the earlier findings that an  $r^5$  function with 6 parameters was the best fit for the curvature of the data. We wanted to investigate how changes in angle affected the measurement of true distances versus the fish-eye distortion, but we understood that the curvature of these points should give rise to a simpler function, which became the focus of our current research.

### 3 In Air Analysis

In an effort to reduce the number of adjustable parameters we looked for other possible fits to compare with the  $r^5$  functional form. We found three possible fits for the raw data,  $r^3$ ,  $r^5$ , and a damped exponential function. Based upon the number of parameters and the errors for each fit at the median measured distance, we concluded a corrected exponential fit would be a plausible fit for the data as shown in Figure 7.

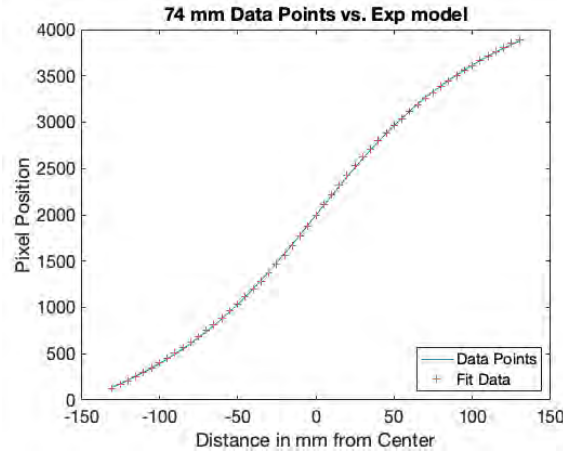


Figure 7: The plot shows the fit point values plotted with the raw data points as the blue line for the exponential model.

Both the errors in the  $r^5$  fit and the exponential fit had comparable ranges in pixel error. This allowed us to use either function, and the ease of the exponential model, with its probable single parameter for distance, won out. We could now use the exponential,  $Pixel = Center + Slope \cdot (1 - e^{-|\frac{x(d) - \mu(x(d))}{width(d)}|}) \cdot sign(x - \mu)$ , where  $Center$  and  $Slope$  are in pixels,  $x$  and  $\mu$  (the mean of  $x$ ) are integers corresponding to the number of 5 mm vertical crossings with the center horizontal axis, and  $width$  is the parameter that changes with distance, to estimate the data points. The subsequent step was to mitigate errors associated with using the exponential function.

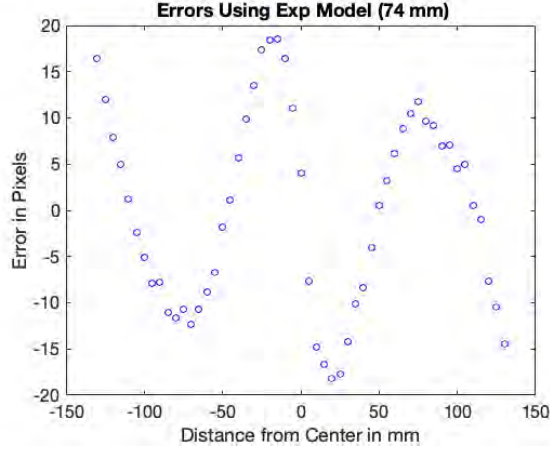


Figure 8: The plot shows the pixel difference of the fit functions versus the raw data collected in order to exhibit the viability of using the exponential fit with fewer parameters. The same was done for the 37 *mm* and 148 *mm* distances.

Figure 8 illustrates the error (in pixels) associated with using the exponential function. The functional form for the sinusoidal fit of errors associated with using the exponential for each distance was  $Error = A \cdot \sin((y-b) \cdot \frac{2\pi}{c})$ , where  $A$  is the amplitude,  $y$  is the raw data in pixels,  $b$  is wavelength in pixels, and  $c$  is the frequency in pixels. We noted that each pixel value has a corresponding hash number. The preceding plots show hash number versus error in pixels. We measured pixels-per-5 *mm* for each distance and compared that to the errors in pixels and decided we needed to adjust our fit function to reduce the residuals of the fit and raw data.

We attempted to mitigate the error in the fit function by fitting the errors to a sinusoidal function and adding the fit data back into the exponential fit function data points in an effort to match the original data. Figure 9 shows the raw data versus the adjusted exponential fit. The fits were done on each of the three distances to target.

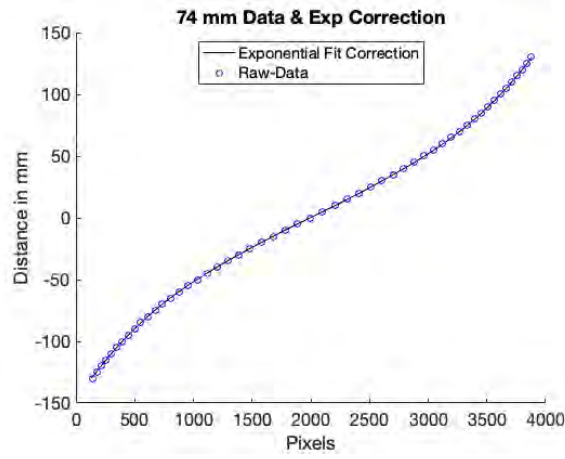


Figure 9: The plot shows the raw data versus the corrected exponential fit. We made the correction by adding the errors from the exponential fit back into the fit point-wise. The graphs also show the one-to-one nature of pixel position and true distances. A flat image would have a linear relationship as opposed to our exponential fits.

From here we calculated the residuals of the corrected exponential, seen below in Figure 10.

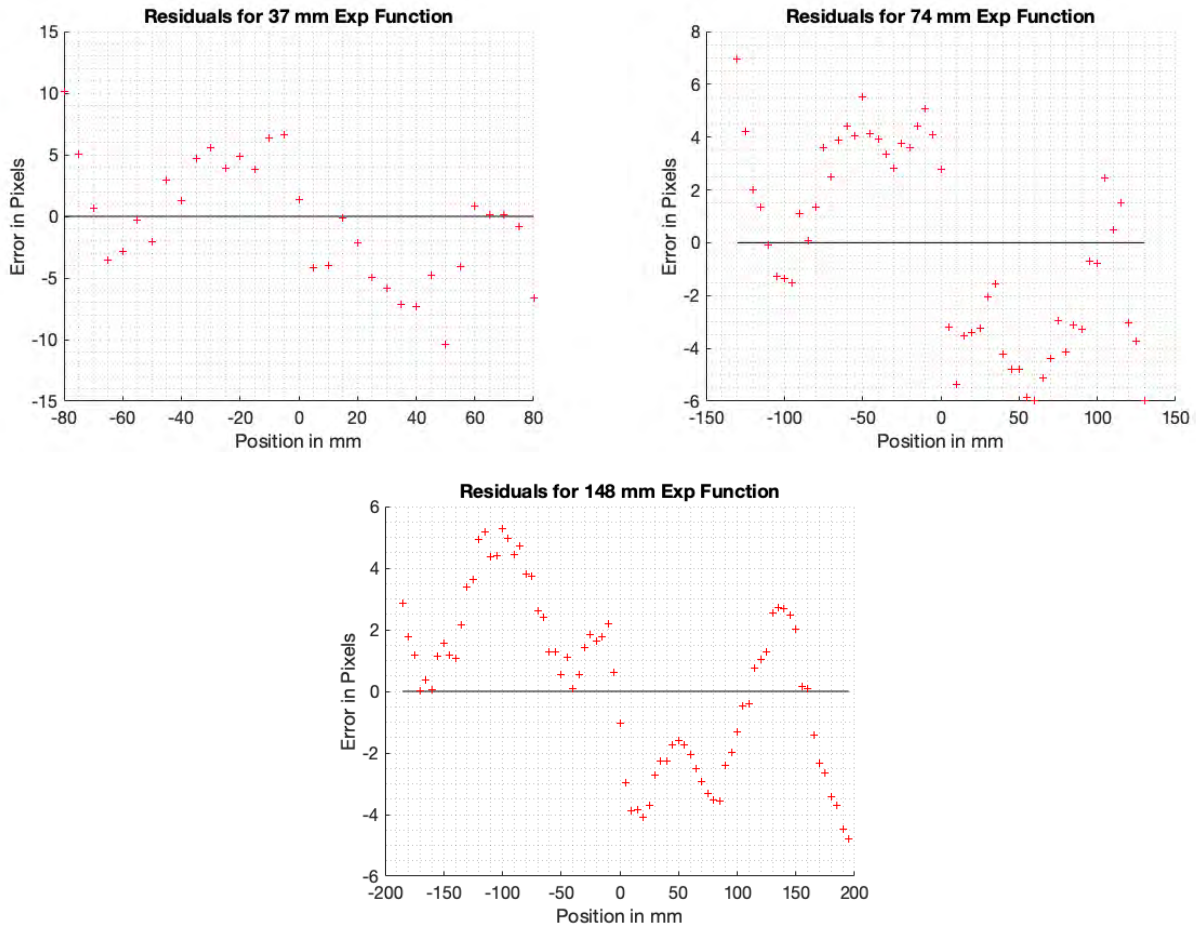


Figure 10: The plots show errors now associated with the raw data versus the corrected exponential fit.

We saw from the plots in Figure 10 that the errors in our fit function to raw data have decreased. In order to examine how effective our error correction was, we had to compare the original error versus our corrected error directly.

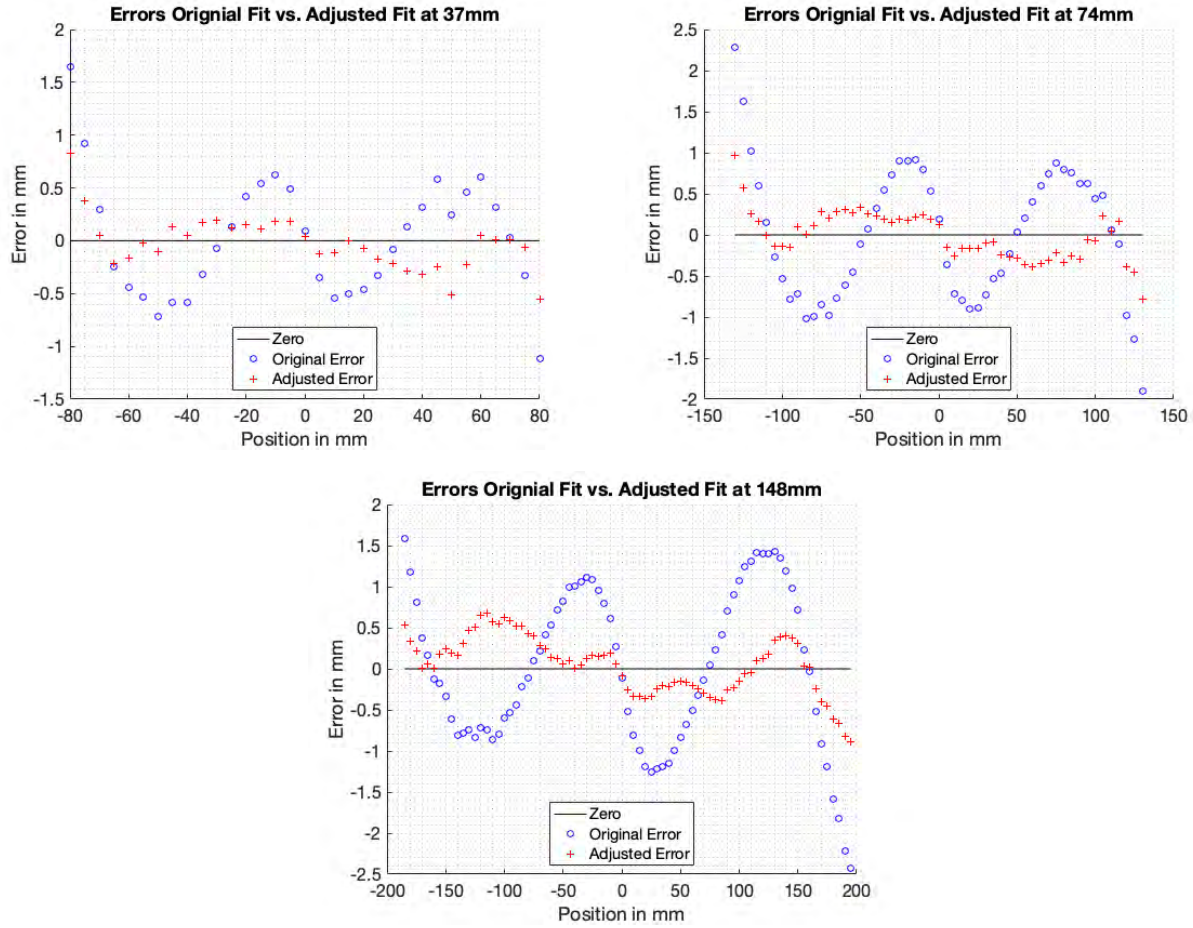


Figure 11: The scatter plots show the two different errors associated with the first exponential fit (in blue) and the adjusted exponential fit (in red). Only a handful of points are farther from zero error after the correction than before, but the amount of difference between the two is negligible.

As seen in the scatter plots of Figure 11, above, the average error in the adjusted exponential fit is less than the error in the original exponential fit for every distance from the target. The position values where the error grew after correction can be ignored because 1) the error in millimeters is negligible to true distance from center, and 2) the variation of the error was greatly improved, thus giving us a tighter range for our known error in the fit.

The result of an adjusted exponential fit to our raw data is a general equation:

$$y - A \cdot \sin((y - b) \cdot \frac{2\pi}{c}) = C + S \cdot (1 - e^{-|\frac{x-\mu}{w}|}) \cdot \text{sign}(x - \mu) \quad (1)$$

$$A = -.04825d + 18.18$$

$$b = -1.648d + 2987$$

$$c = -2.882d + 1893$$

$$C = .1776d + 1999$$

$$S = 1.021d + 2832$$

$$\mu = (8.299 * 10^{-4})d + .4148$$

$$w = 1.532d + 12.15.$$

On the left side of the equation,  $y$  is pixel value, and on the left side of the equation,  $x$  is the distance in  $mm$  from the center of the image,  $0\text{ mm}$ . The variable  $d$  in the linear equations is the distance in  $mm$  between the camera and the target plane. The next step was to examine angle corrections to the in air data. Before doing so, we decided to attempt to characterize image curvature using video settings with the lens submerged.



## 4 Submerged Lens Procedure

To best test the behavior of the lens while submerged in water, we laminated the graph paper and placed the target to the same distances from the lens as in air. We then filled a plastic bin with water to the point of submerging the lens and proceeded to take video images from each distance,  $37\text{ mm}$ ,  $74\text{ mm}$ , and  $148\text{ mm}$ . The process continued as with the in air imaging and immediately we realized the fisheye images had been corrected to being linear, as seen in Figure 12.

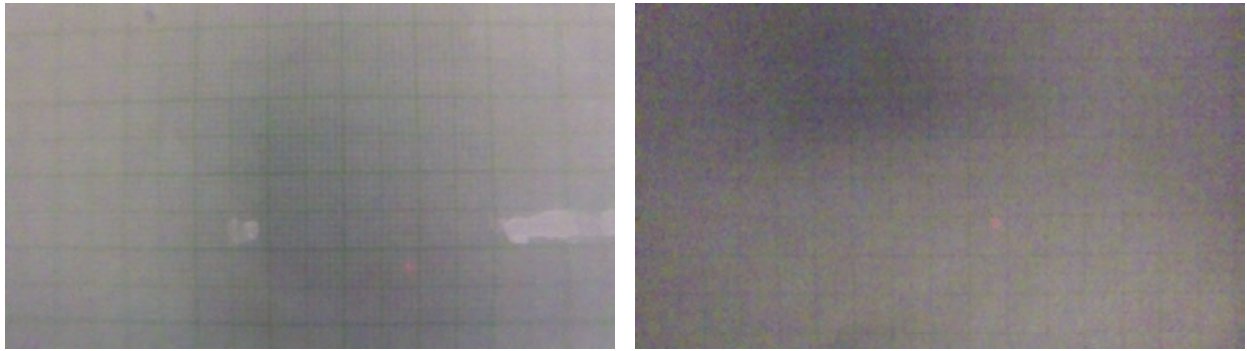


Figure 12: These images show distances of  $37\text{ mm}$  (left) and  $74\text{ mm}$  (right) with the camera lens and target submerged.

In order to discern the pixel per millimeter values for a given distance we fit the data points to a line and extracted the slope for each distance measured, as seen in Figure 13. The linear model fit's error was on the order of  $.5\text{ mm}$  at the edges and barely discernible in the center of the field of view, where recording would take place. After we found the scale length in the submerged images to scale as  $\frac{1}{d}$ , also seen in Figure 13, we could then begin to construct a dark region in which to record our particle motion.

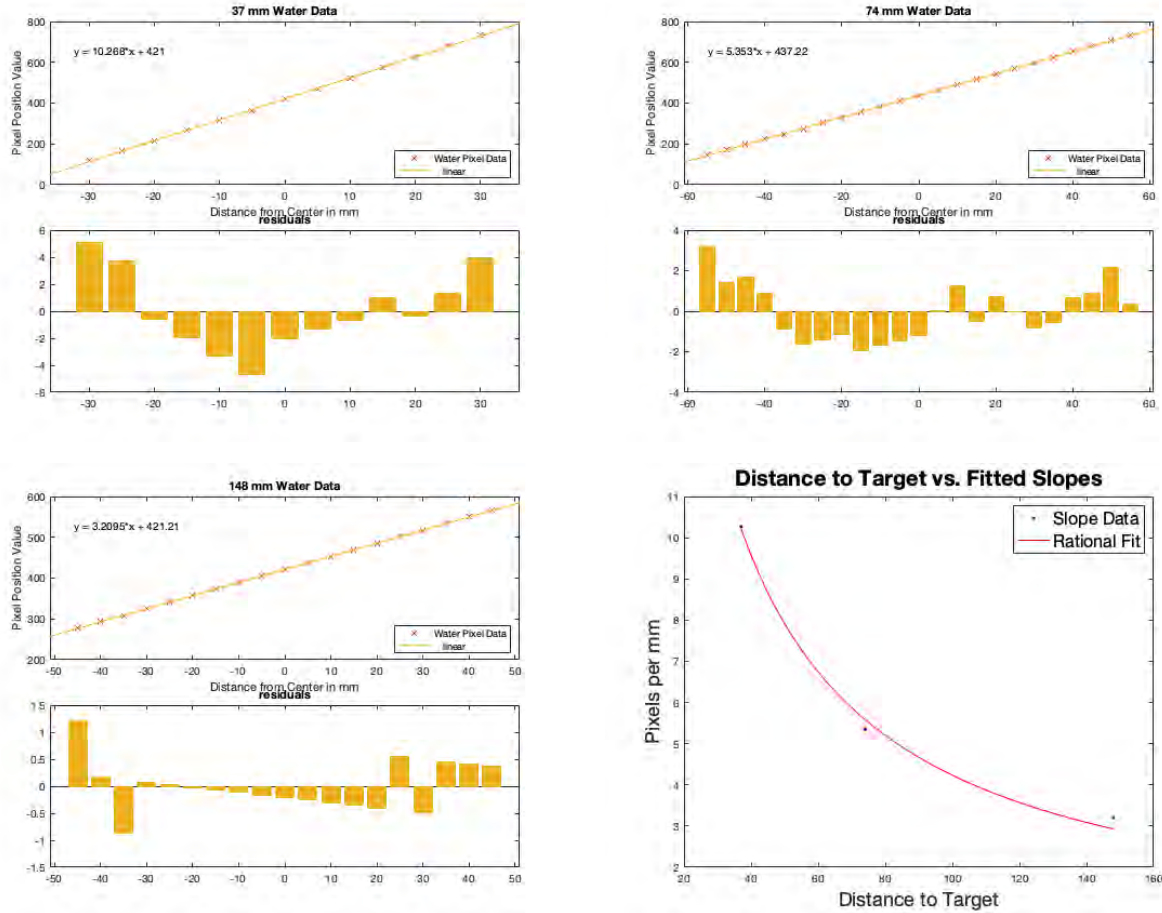


Figure 13: These images show linear fits of 37 *mm* (top left) and 74 *mm* (top right) and 148 *mm* (bottom left). The rational fit curve (bottom right) allowed for an understanding of the conversion from pixels to *mm*.

We used a red HeNe laser with a 1 *mm* diameter beam to illuminate an area of the water adjacent to the teeth of a saw blade. We then mounted the camera above the submerged blade in a manner such that the lens was also submerged and parallel to the plane of the blade. We then tried to image the motion of rosin particles (pine sawdust and turpentine) chosen for their near neutral buoyancy. Figure 14 shows the general dimensions of a typical buoyant particle. Both rosin particles are on the order of .6 *mm* in diameter at their widest point. Rosin that was larger than 1 *mm*, tended to sink, as its density made it no longer buoyant. Particles much smaller than this could not break surface tension.

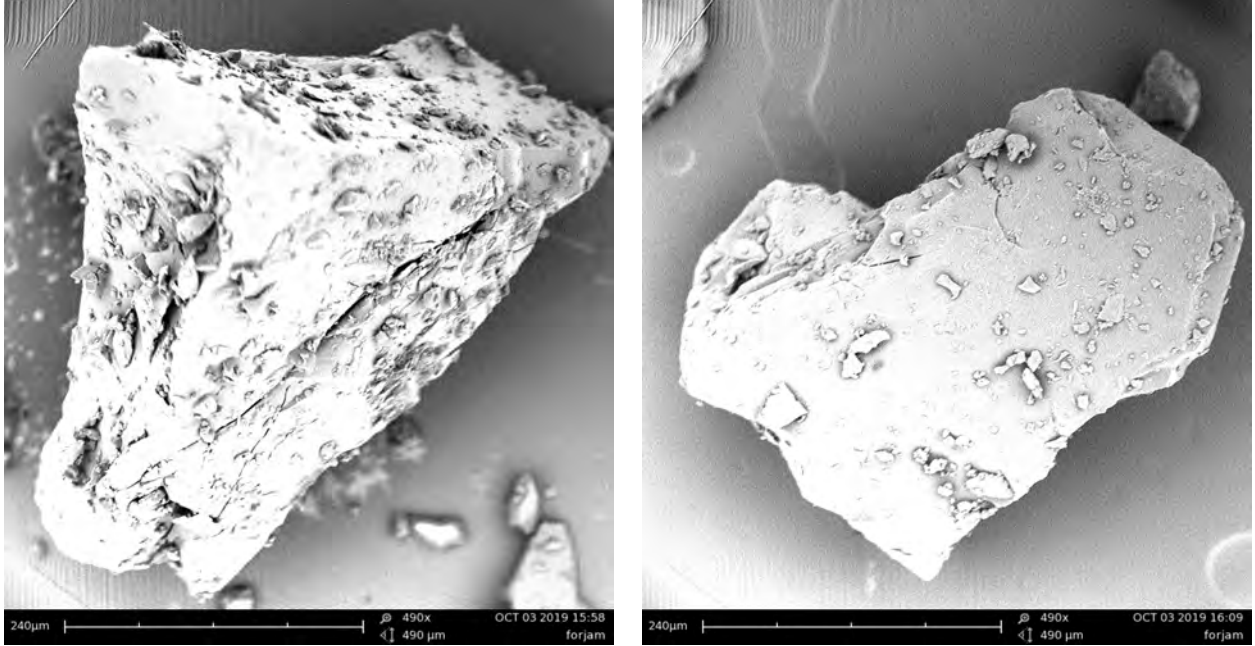


Figure 14: These images show the size and shape of the buoyant particles. While the surfaces are not smooth nor is a typical particle perfectly round, their reflected output was circular once thresholded.

We then took video of particles falling and moving as they would with no driven oscillations to understand the rate at which a typical particle would travel due to only the force of gravity. Larger particles, over 1 *mm* in diameter were put on the surface of the water and allowed to freely fall as we recorded. After waiting for particles to enter the frame, we found particle motion under these conditions to be on the order of 4 *mm* per second. We then attempted to do the same measurements for an oscillating system.

Initially, it was difficult to see enough particles for any measurements so we decided to increase the concentration of particles in the water, shown in Figure 15 below. In doing so we were able to finally see a bevy of particle motion.



Figure 15: This image shows the yellow rosin particles that were too small to break surface tension. Those too large to be neutrally buoyant naturally sink, while the neutrally buoyant particles drift submerged at various levels in the fluid.

We decided it best to increase the diameter of the beam to  $4\text{ mm}$  using two convex lenses to better capture particle motion. As with all fluid dynamic systems, dimensions are important. We decided to use a standard wood saw blade for our test blade. The blade was  $32.5\text{ mm}$  long and  $.7\text{ mm}$  thick, with teeth whose tips measured  $1\text{ mm}$  apart as can be seen in Figure 16.



Figure 16: This image shows the wood blade we used in the experiment. Its dimensions were similar to those of the saw blade used by experimenters in the past to cut algae.

Once the final setup was established we took a series of videos with the oscillating saw at 2880 oscillations per minute, roughly  $48\text{ Hz}$ . Using the WiFi from the GoPro, we were able to record a series of videos accounting for different periods in the flow. From this point we used MATLAB for image processing.

We chose a video of the proper length to observe multiple single particle behavior. Since the video was mostly black with a red laser illuminating the particles, we were able to isolate the red channel and set it to gray scale. Figure 17 shows the same frame extracted from a video, first as is and second in grayscale for the isolated red channel.

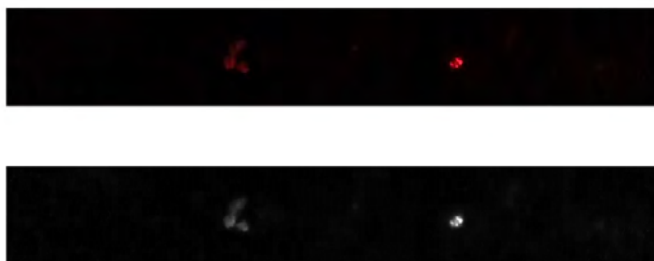


Figure 17: The top image is the raw frame data from our video, where as the bottom image shows the same frame with the red channel isolated and set to grayscale.

In frames 341 – 357 of the video, we were able to isolate a particle and obtain the region properties by setting a threshold value. Thresholding refers to the tightening of the range of index values allowed in a given region. An analysis of potential threshold values, shown in Figure 18, showed values above 20 to be the most appropriate thresholding value.

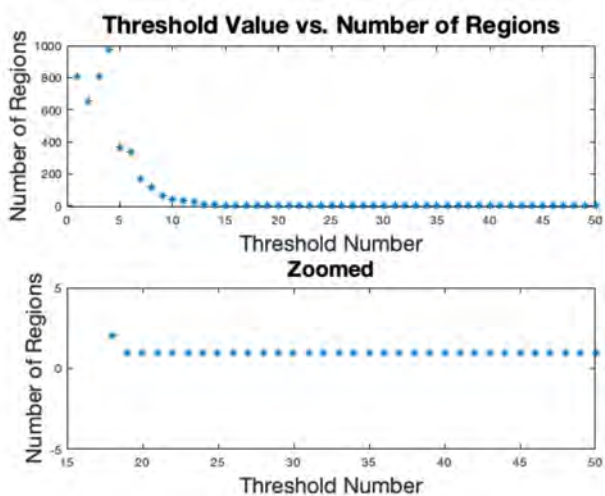


Figure 18: The top image is the raw frame data from our video, where as the bottom image shows the same frame with the red channel isolated and set to grayscale.

In order to narrow down the threshold region, a frame was chosen with a known number of particles, and visual inspection was used to match thresholded images to the original gray-scale. Figure 19 shows the original gray-scale along with threshold values of 10, 15, 20, 25, and 30.



Figure 19: The top image is the gray-scaled data from our video. The subsequent pictures are threshold values in increments of 5 starting with a value of 10. While noise cancellation occurs by 20, a value closer to 25 was chosen to optimize the algorithm.

The noise present in this frame is mitigated after a threshold of 20, as expected, and the value of 30, while still visually accurate, begins to separate a known particle into two regions. The value of 24 was settled on to allow for the separation of two close particles, while still keeping a single particle as one region. Once a threshold value was established, we were able to use MATLAB to further analyze our data.

MATLAB's region properties use the 8-connected pixels to a tested pixel to determine borders in binary images. If a true value, 1 is returned, then the pixel has color in a given index ranging from 0 to 255. The use of 8-connected pixels means pixels are connected if their edges or corners touch, as shown in Figure 20.

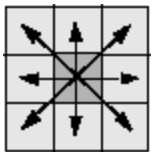


Figure 20: A visual representation of what it means for a region to be connected. The edges and corners must have positive boolean values to be a part of a pixels region.

Two adjoining pixels are part of the same region if they both return true values and are connected horizontally, vertically, or diagonally. Region properties in MATLAB returns many values such as area, centroid, bounding box, and equivalent diameter that we would use to automate the particle tracking process.

Initially, we analyzed the motion of a bright particle manually by frame. We calculated mean value location for an indexed pixel value and tracked those points for the seventeen frames. We then did the same analysis with centroid data and showed the centroid of the bright area to be a more accurate representation of the particles movement.

Next, we turned to writing an algorithm that could automate that process and return similar results. The algorithm took into account the areas of any white blobs that appeared in the frame. If the area was above a given value, in our case 36 pixels, then the blob's centroid put into one array while a smaller area's centroid was put into another array. Larger areas were marked with a red *X* and if the area was less than 36 pixels, a blue star, as shown in Figure 21. We then plotted the two arrays of centroids superimposed upon the gray-scaled frame, and then compiled that data back into a short video to test for alignment of the data. The centroids for any blob appearing in the video are now visible divided into two arrays based upon size. Figure 21 also shows the centroid accurately moving with a known particle.





Figure 21: These frames show the centroid value for a region of a given area and how the centroid tracks over a number of frames

For the purpose of a fully automated tracking algorithm, a cell array was created with all centroid values that could then be referenced versus a potential radius of movement to track a region from frame to frame. This algorithm is still under construction as of the writing of this report.

## 5 Submerged Lens Analysis

Two ranges of frames were observed and run through the algorithm. Frames 341–357 and frames 1640–1667 from one of the longer videos taken were put through the algorithm and the manually chosen particles' centroid data was plotted. An average velocity taken between the two points was taken and frames 341–357 can be seen in Figure 22.

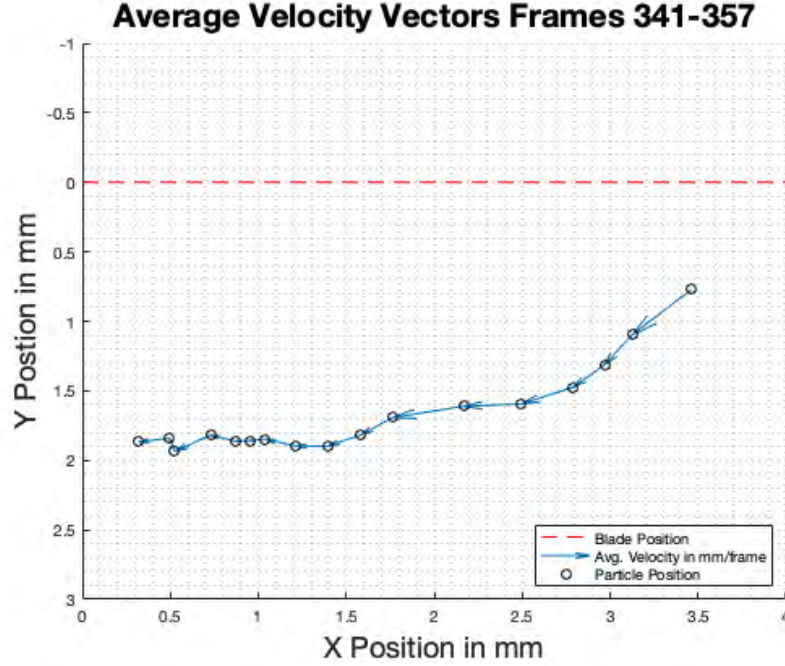


Figure 22: The particle followed through these frames (341 – 357) took the path marked out by the blue velocity arrows. The average  $x$  velocity over the frames was about three times greater than the average  $y$  velocity over the frames observed.

The average  $x$  velocity for this particle was roughly three times the average  $y$  velocity. Since the blade was oscillating predominately in the  $x$  direction, this was expected. We then analyzed the continuity equation for an incompressible fluid,  $\nabla \cdot \vec{V} = 0$ , where  $\vec{V}$  is the velocity vector of the particle along the pathline. In Figure 23, we see a plot of the separate components of the continuity equation.

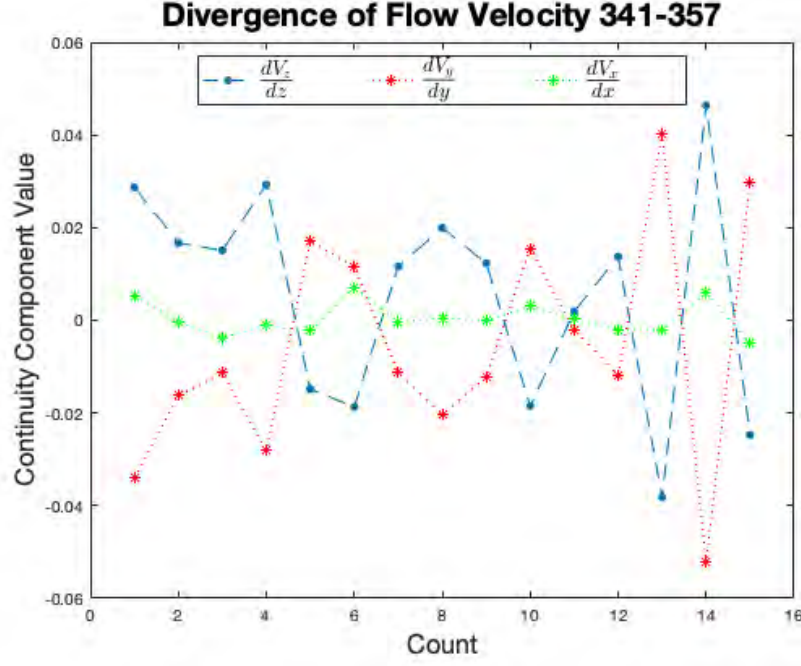


Figure 23: In this figure, the green and red values for the divergence of the velocity were measured values. Through the continuity equation,  $\frac{\partial V_z}{\partial z}$  was calculated and is shown in the dashed blue line.

We noticed the  $\frac{\partial V_x}{\partial x}$  component of the divergence contributed very little to the overall divergence. This meant the change in  $x$  velocity over the life of the pathline was very little. Conversely, the  $\frac{\partial V_y}{\partial y}$  and  $\frac{\partial V_z}{\partial z}$  components oscillated much more over the course of the pathline. The oscillation is most likely attributed to a combination of the oscillatory motion of the blade and motion through vortices in the  $y - z$  plane. The larger values for the two components relative to the  $x$  component and their change from positive to negative suggest a spiraling motion to the flow in both the  $y$  and  $z$  direction. Since the tracked particle did not show a change in basic shape or contour when manual viewed, this change not due to rotation about the center of mass of the rosin, but the rotation of the fluid. This was evidence in favor of turbulent fluid flow, but the periodicity of the divergence also suggests some structure. The Reynolds number would properly characterized the fluid flow.

In order for fluid flow to be fully turbulent, the Reynolds number must be on the order of  $10^6$ . The Reynolds number at the blade was calculated as a function of the frequency,  $48 \text{ Hz}$ , and blade length plus its total displacement,  $48.5 \text{ mm}$ . This gave a Reynolds number of 126,863. This is high enough to be turbulent but not to the  $10^6$  to be chaotic turbulence. A Reynolds number at  $10^5$  would still exhibit some structure

to the flow.

When we calculated the Reynolds number using the dimensions of the entire system, 540 *mm* in the *x* direction and 300 *mm* in the *y* direction, the particle tracked in frames 341 – 357 had a Reynolds number of 27,303 in the *x* direction and 5,710 in the *y* direction. These values would put the particle in the turbulent domain, but not full fledged turbulence. However, when we took the conservative approach of the *x* length scale being blade width plus total blade displacement in the *x* direction and the *y* length scale as particle displacement plus total blade displacement in the *y* direction, the Reynolds numbers were 2,452 in the *x* direction and 76 in the *y* direction. This seemed to suggest particles at this distance from the blade have transitioned back from turbulence to a more laminar flow.

The next pathline tracked occurred in frames 1640 – 1663. The reason for the abbreviation over the last four frames was one particle overtaking another on a similar pathline. This lead to a possibility for turbulence since two particles in nearly the same location had different velocities. In order to quantify this assumption, we tracked one of the particles in a similar fashion as the earlier frames to understand its dynamic properties. Figure 24 shows the pathline for the particle observed.

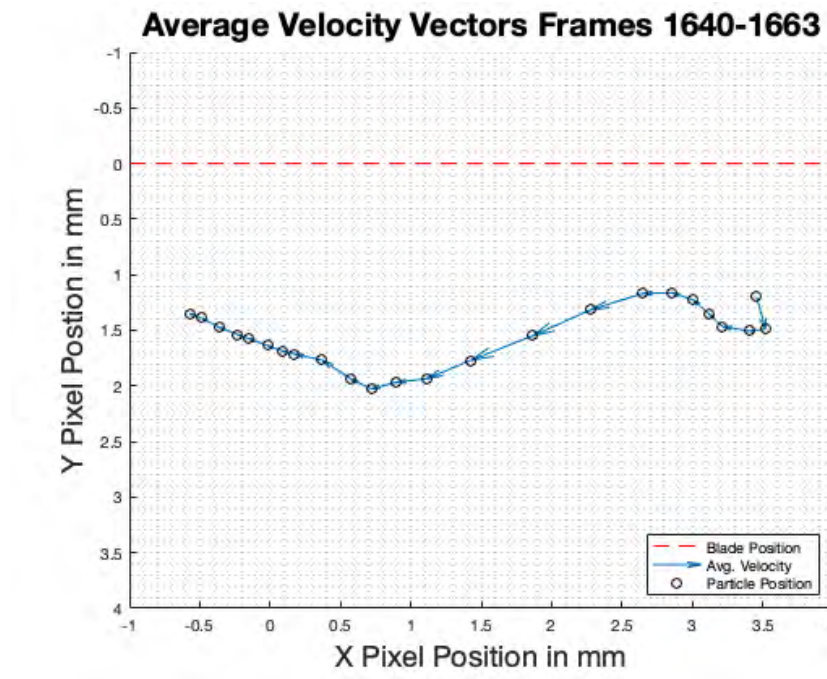


Figure 24: The particle followed through these frames (1640 – 1663) took the path marked out by the blue velocity arrows. The average *x* velocity over the frames was again greater than the average *y* velocity over the frames observed.

Once again, using the entire system's dimensions as a length scale, the Reynolds number associated in the  $x$  direction was 24,876 and 4,719 calculated in the  $y$  direction. When the more conservative length scales were used to calculate the Reynolds numbers, they were 2,234 in the  $x$  direction and 63 in the  $y$  direction. As before, we saw evidence of a return to a laminar flow state from the turbulent mixing that occurred at the blade.

Looking once again at the divergence of the velocity, we saw another oscillatory pattern, shown below in Figure 25.

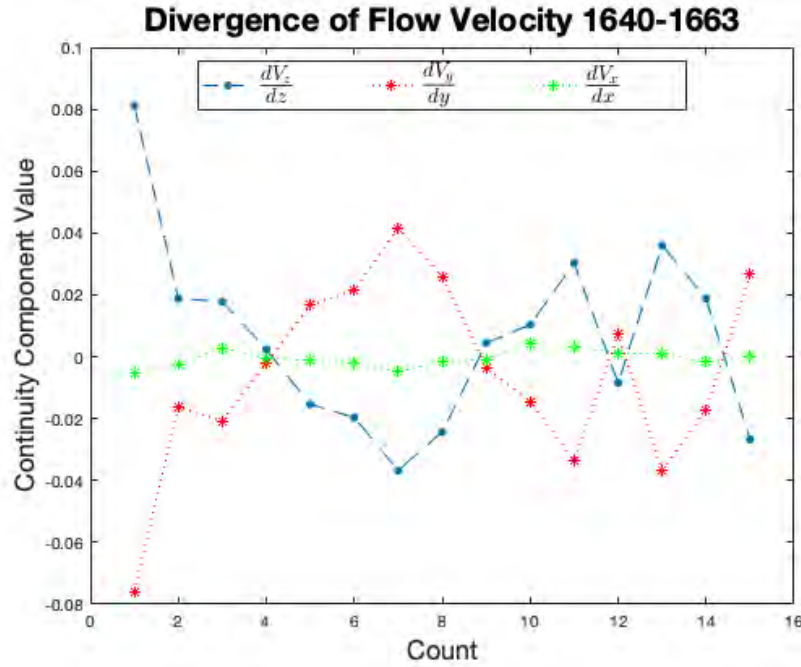


Figure 25: As in the previous divergence figure, the green and red values for the divergence of the velocity were measured values. Through the continuity equation,  $\frac{\partial V_z}{\partial z}$  was calculated and is shown in the dashed blue line.

As before this is evidence of possible turbulent flow on its own, and when coupled with high enough Reynolds numbers, we have shown structured yet turbulent flow. However, when we looked at a smaller region of the system, we found the high laminar values to match the patterned structure of the divergences. These facts suggested a transition back to the laminar regime from the turbulence at the blade itself. Once the tracking process becomes automated, we would show the ability to further characterize the flow for many particles within the same frame.

## 6 Future Work

We understand a full fluid dynamic study of this system is a large undertaking. The automation of the tracking algorithm will allow many particles to be track from frame to frame. From there, one can do a statistical analysis on all the particles to characterize a general flow through the viewing region. We would then repeat the experiment and find values for various distances from the blade in order to better characterize any turbulent like flow as a function of distance from the blade. Ideally we could classify the flow in all three dimensions through the single camera setup, but extrapolating from the divergence equation allows us to classify the flow in such a way that we may be able to successfully cut algae based only on empirical two dimensional data.

After fully automating the tracking system and finding the flow patterns as a function of distance for this particular blade, we would then work on blade design optimization. This would be a combination of tracking and flow classification along with cutting attempts in order to better understand which level of turbulence best suits our desired goal of in water algae harvesting.

## 7 Conclusion

In summary, the project has achieved the following milestones: accurate distance measurements within a distorted image, the ability to adjust the measurements based on distance from target plane both in and out of water. In air we are able to make accurate distance measurements within a fisheye distorted image due to the exponential fit of data points. In water , the distances scale as  $\frac{1}{d}$ . Using the knowledge of these two fit functions, we are able to express distances in an image based upon the cameras distance from the target plane. We know that the change in our functional value scales linearly with distance for the in air camera.

For the purpose of our project we have eliminated the need to understand angle deviations in distance, since distances are linear with a submerged lens. This allowed us to make the necessary measurements to draw conclusions about the flows from an oscillating blade. We are also able to make accurate two dimensional analyses of particles in fluid flow. In order to do so we have optimized an algorithm to manually track particles throughout a video. It is only a programming step to fully automate the experiment.

Finally, we understand now that oscillations at 48  $Hz$  create flows that are in the turbulent domain but

do transition back to laminar flows at the distances particles were observed from the blade. The turbulence seen at the blade was within the turbulent domain that had not yet reached chaotic motion, where the original experimenters believed the algae would best be cut. We have found an accurate way to assess the speeds associated within that region, and through Reynolds numbers we are able to scale to the full meter sized blade once the optimal blade design is found through further experimentation.

## 8 References

Figure 2. Mirasol-Menacho, Sebastin & Planells-Prez, Ana & Barba-Sevillano, Arturo & Segura Garcia, Jaume & Cobos-Serrano, Mximo & Gimnez, Alicia. (2016). Development of a HMD for Virtual Acoustics. Application in a World Heritage (UNESCO) Building from the Valencian Civil Gothic. 241-250.

Cooke, William E, and Katherine Davis Small. Algal Aqualculture for Nutrient Assimilation and Removal. 2015

Manos, Dennis, and William Cooke. Algal Biomass Production System Final Report. 2011

Muscari, Roberto, et al. "Modeling of Vortex Dynamics in the Wake of a Marine Propeller." *Computers & Fluids*, vol. 73, 2013, pp. 65-79., doi:10.1016/j.compfluid.2012.12.003.

Sutton, Elizabeth J., et al. "Cell Tracking with Optical Imaging." *European Radiology*, vol. 18, no. 10, 2008, pp. 2021-2032., doi:10.1007/s00330-008-0984-z.

Wang, Lian-Zhou, et al. "A Numerical Study on the Correlation between the Evolution of Propeller Trailing Vortex Wake and Skew of Propellers." *International Journal of Naval Architecture and Ocean Engineering*, vol. 10, no. 2, 2018, pp. 212-224., doi:10.1016/j.ijnaoe.2017.07.001.